

See discussions, stats, and author profiles for this publication at: <https://www.researchgate.net/publication/333786954>

Prediction of MRI RF Exposure for Implantable Plate Devices Using Artificial Neural Network

Article in IEEE Transactions on Electromagnetic Compatibility · June 2019

DOI: 10.1109/TEM.2019.2916837

CITATIONS

0

READS

107

4 authors:



Jianfeng Zheng

University of Houston

74 PUBLICATIONS 687 CITATIONS

SEE PROFILE



Qianlong Lan

University of Houston

19 PUBLICATIONS 54 CITATIONS

SEE PROFILE



Xingyao Zhang

University of Houston

7 PUBLICATIONS 24 CITATIONS

SEE PROFILE



Wolfgang Kainz

U.S. Food and Drug Administration

140 PUBLICATIONS 2,727 CITATIONS

SEE PROFILE

Some of the authors of this publication are also working on these related projects:



MRI RF heating [View project](#)



Virtual and Remote Laboratory (VR-Lab) Development [View project](#)

Prediction of MRI RF Exposure for Implantable Plate Devices Using Artificial Neural Network

Jianfeng Zheng¹, Member, IEEE, Qianlong Lan, Xingyao Zhang, Wolfgang Kainz², Member, IEEE, and Ji Chen¹, Senior Member, IEEE

Abstract—The purpose of this paper is to present a fast method to predict the radio frequency (RF) exposure for multi-configuration implantable devices in the magnetic resonance imaging (MRI) environment by using an artificial neural network (ANN). A synthesizing framework is developed to improve the ANN, of which the inputs are the geometric dimensions of the targeted device and the output is the peak 1-g average SAR (SAR_{1g}) of the device. The synthesizing framework integrates feature selection and performance optimization techniques, achieved by using the mean impact value (MIV) algorithm and genetic algorithm (GA), to identify the most impactful features and improve the performance of the ANN. The framework was implemented and validated with the samples of 576 implantable plate devices with various geometric dimensions. The dimensions of the device were determined by six parameters and the peak SAR_{1g} of the devices was numerically calculated by using a full-wave electromagnetic solver based on the finite-difference time-domain method. The efficiency and accuracy of the proposed framework were systematically evaluated. Comparing with the unimproved ANN, the mean square error (MSE) of the predicted peak SAR_{1g} decreased by 28.06% for the ANN using MIV algorithm, while the MSE decreased by 55.29% for the presented synthesizing framework. The MSE of the predicted peak SAR_{1g} was $8.16 \text{ W}^2/\text{kg}^2$ and the correlation between the predicted and calculated peak SAR_{1g} was 0.994 for the improved ANN in the studied cases.

Index Terms—Artificial neural network (ANN), genetic algorithm (GA), magnetic resonance imaging (MRI) safety, mean impact value (MIV), radio frequency (RF) induced heating.

I. INTRODUCTION

IMPLANTABLE devices are widely used in clinical treatments to diagnose damaged biological tissues or structures. Meanwhile, implantable devices, especially with metallic materials, are usually contraindicated during magnetic resonance imaging (MRI) procedure, which is one of the most capable, safe, and widely used medical imaging technique. When patients with implantable devices undergo MRI procedures, the radio frequency (RF) exposure due to the interactions between

implantable devices and MRI RF coil may cause tissues burns [1], [2]. Recently, the MRI RF exposure for some implants has been carefully studied to clarify the MRI safety conditions, and patients with these devices can proceed to the MRI scan in fully controlled environments following these conditions [3]–[10]. For passive implantable devices, the MRI RF exposure is assessed in a standard way per the American Society for Testing and Materials (ASTM) standard F2182-11a [11]. This assessment needs costly measurements or numerical simulations which can take relatively long time. Therefore, it is not applicable in many scenarios, such as providing the MRI RF exposure of all available configurations for diverse device configurations, for fast predicting the MRI RF exposure in the design stage, or estimating the potential risks for patients with unlabeled implantable devices in emergency situations, etc. A commonly used multi-configuration implantable device can have thousands to millions of different configurations to cater clinical requirements, thus brute-force one-by-one RF-induced heating assessment is too costly and almost infeasible. A complexity-reduced method was suggested in [12], but the method cannot provide MRI RF exposure for each configuration and may underestimate the possible worst case situation [13], [14].

A preliminary study has been presented to demonstrate the validity of using an artificial neural network (ANN) to predict the MRI RF exposure for the implantable plate system [15]. It was observed that the ANN is a potential solution to the MRI RF exposure prediction problem with non-linear and high-dimensional features [16], [17]. However, the convergence and performance of the presented ANN, which depends on the heuristically selected configurations of the network, were not guaranteed in the previous studies, and the number of studied samples was also limited.

When building an ANN, one of the major challenges is to determine the input of the ANN, which can be the significant features of the target subjects. The missing of noteworthy features may lead to poor performance in terms of prediction accuracy, while too many minor features can result in divergence of the ANN, especially when only a limited scale of training data is available. Because it is difficult to heuristically extract the most impactful features of the devices for the ANN, the mean impact value (MIV) algorithm [18] is used as the feature selection technique to decide the inputs of the ANN.

In addition, heuristically selected configurations of the ANN, such as random initial weights and bias, may introduce two major drawbacks: the local minima dilemma and a slow convergence

Manuscript received July 18, 2018; revised November 10, 2018 and March 1, 2019; accepted March 26, 2019. (Corresponding author: Jianfeng Zheng.)

J. Zheng, Q. Lan, X. Zhang, and J. Chen are with the Department of Electrical and Computer Engineering, University of Houston, Houston, TX 77204-4005 USA (e-mail: jason.zhjf@gmail.com; lq11254@gmail.com; zhangxyleo2013@gmail.com; jchen18@uh.edu).

W. Kainz is with the Center for Devices and Radiological Health, Food and Drug Administration, Rockville, MD 20852 USA (e-mail: wolfgang.kainz@fda.hhs.gov).

Color versions of one or more of the figures in this paper are available online at <http://ieeexplore.ieee.org>.

Digital Object Identifier 10.1109/TEM.2019.2916837

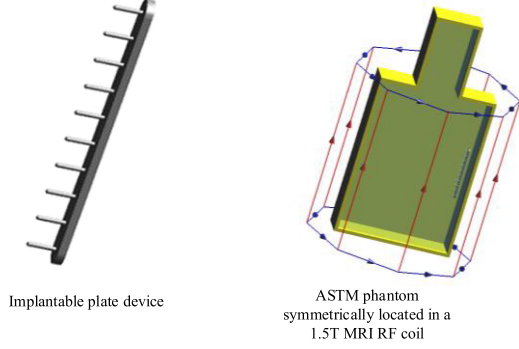


Fig. 1. Implantable plate device and ASTM phantom symmetrically located in a 1.5 T MRI RF coil.

TABLE I
PARAMETERS OR FEATURES OF THE IMPLANTABLE MEDICAL DEVICES

No.	Features	Values (mm)	Number of Values
1	Plate Length	100, 140, 180, 220, 260, 300	6
2	Plate Width	10, 20	2
3	Plate Depth	3, 5	2
4	Screw Length	20, 40, 60	3
5	Screw Diameter	1, 3, 5, 7	4
6	Distance to 1 st Screw	10, 20	2

The total number of available configurations is $C_6^1 \times C_2^1 \times C_2^1 \times C_3^1 \times C_4^1 \times C_2^1 = 576$.

[19]. It is necessary to make sure of the ANN convergence even there are few training data. Thus, the genetic algorithm (GA) [20] is adapted as the optimization tool to optimize the ANN by adjusting its initial weights and bias.

The synthesizing framework is presented to build the efficient and reliable ANN, which consists of three stages: 1) build and train an initial ANN with heuristically determined structures; 2) deploy the MIV algorithm to select the most impactful and important implant features; and 3) apply the GA to search for the optimal connection weights and biases, which will be used as the connection weights and biases of the final ANN.

The remainder of this paper is organized as follows. In Section II, simulations of the peak 1-g average SAR (SAR_{1g}) for the example implantable devices are presented. Section III introduces the initial ANN architecture, and Section IV presents the feature selections using the MIV algorithm. The optimization of initial weights and biases using the GA is presented in Section V. Section VI focuses on validating the results of the ANN. Conclusions are presented in Section VII.

II. NUMERICAL SIMULATIONS OF THE PEAK SAR_{1g}

Generic implantable plate devices were used as the studying samples, which were composed of a flat plate and several screws as showed in Fig. 1. The generic plate devices can represent the widely used implantable devices for bone trauma and fracture treatments. The features of the plate devices are given in Table I. The plate has a length of 100–300 mm with an interval of 40 mm, and a width of 10 or 20 mm. The screw has a length of 20–60 mm

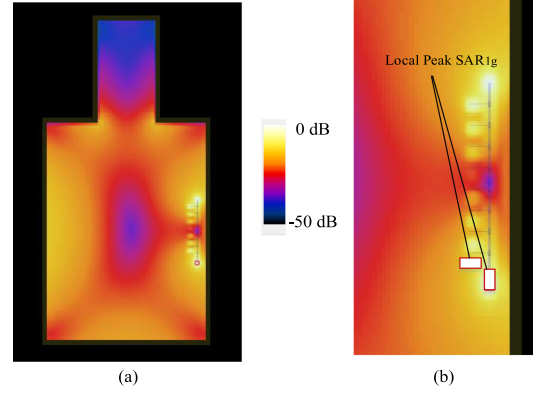


Fig. 2. (a) Implantable medical device was placed in the middle of the phantom in the bore direction and 2 cm away from the longest side wall. (b) Local peak SAR_{1g} near two possible hot spots.

with an interval of 20 mm, and diameter of 1–7 mm with an interval of 2 mm. The distance from the first screw to plate tip is 10 or 20 mm. The material of the plate device was metal, modeled as perfect electric conductor (PEC). In this study, a total of 576 plate devices were constructed, and the MRI RF exposure of the devices was calculated in terms of the peak specific absorption rate averaged over 1 gram (SAR_{1g}) [3].

A. Simulation Setups

Numerical simulations were performed using the full-wave computational electromagnetics software SEMCAD X (V14.8.6, SPEAG) [21] based on the finite-difference time-domain method. A high-pass non-physical RF transmit body coil was adopted to model the MRI RF body coil at 64 MHz and was loaded with a model of the ASTM phantom shown in Fig. 1. Eight current sources were placed on the rungs of the coil to generate a uniform magnetic field inside the coil. Absorbing boundary conditions were used on all sides of the simulation boundaries. The ASTM phantom was a plastic container with a relative dielectric constant $\epsilon_r = 3.7$ and an electrical conductivity $\sigma = 0$ S/m, filled with gelled-saline, which had $\epsilon_r = 3.7$ and $\sigma = 0.47$ S/m. The plate device was placed at the vertical center on the right side 2 cm away from the phantom wall and at the center along the bore direction (the location which provides maximum and uniform electric field exposure inside the phantom), as shown in Fig. 2. In the simulation, all metallic materials were modeled as PEC.

A nonuniform mesh was used in the simulations to approach the balance between accuracy and complexity because the size of the coil, phantom, and device were significantly different. The larger mesh step size can reduce the total simulation time, but a coarse mesh cannot represent small device structures correctly. The smaller mesh step size can give more accurate mesh voxels, but it may cause long computational times and divergent results. With several convergence analyses, we determined that the mesh size of 0.5/1 mm was applied to the plate devices. The mesh size of the gelled-saline was 5 mm and the plastic box was

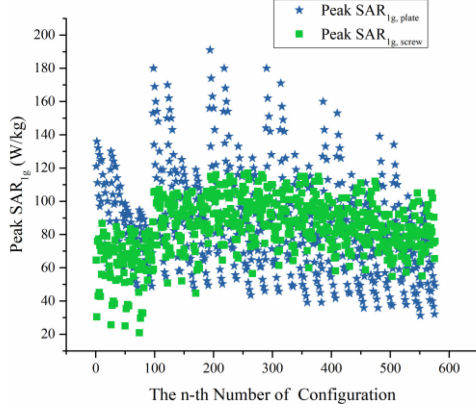


Fig. 3. Simulation results of 576 configurations are obtained by using different combination of parameters or features of the implantable plate devices.

10 mm. The grating ratio of the mesh size was set to 1.15. Simulations were accomplished using the CUDA acceleration feature of SEMCAD-X with the NVIDIA C2075 high-performance graphic processing unit, which was able to run up to 650 million cells per second. Although the high computational capabilities were provided, it still takes approximated 1500 h per computer to get the SAR_{1g} distribution for all configurations. To ensure the convergence, the simulation time was set for 15 periods. In the following study, all the simulation results were normalized to a whole-body average SAR of 2 W/kg.

B. Simulation Results

Numerical simulations were performed to calculate the electromagnetic field distribution, and the distribution of SAR_{1g} for the devices was extracted, as showed in Fig. 2. The orientation of the plate device has significant impacts on the peak SAR_{1g} . The peak SAR_{1g} will decrease when the plate is tilted to the transverse plane. For the sake of conservatism, the long axis of the device was aligned with the electric field (along bore direction) in order to get the highest peak SAR_{1g} . Because the studied plate systems were PEC, the peak SAR_{1g} occurred near the plate end or screw end, where the currents were discontinuous. Specifically, the peak SAR_{1g} among the different plate devices with various parameters was either near the plate end or the first screw end. The simulation results of the 576 configurations of the implantable plate devices are showed in Fig. 3. Each configuration is corresponding to one combination of the parameters from Table I, and each configuration is different from the others. Therefore, the total number of the configurations is $C_6^1 \times C_2^1 \times C_2^1 \times C_3^1 \times C_4^1 \times C_2^1 = 576$. For example, the first configuration will be plate length = 100 mm, plate width = 10 mm, plate depth = 3 mm, screw length = 20 mm, screw diameter = 1 mm, and with distance to the first screw = 10 mm. The simulation results show that the peak SAR_{1g} near the plate is usually higher than the peak SAR_{1g} near the screw. The highest peak SAR_{1g} near the plate (peak $SAR_{1g,plate}$) is under 200 W/kg and that near the tip of the screw (peak $SAR_{1g,screw}$)

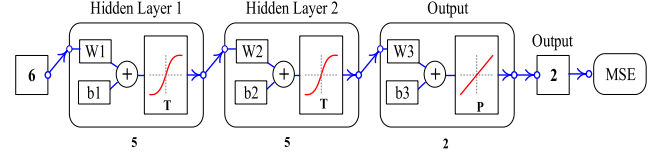


Fig. 4. Architecture of initial ANN consists of six inputs, two hidden layers, one output layer, and two outputs. w_1 , w_2 , and w_3 are the vectors containing the connection weights between the different layers, while b_1 , b_2 , and b_3 are the biases for the different layers. T represents the tan-sigmoid transfer function in (1) and (2), and P represents the Purelin linear transfer function in (3). The final outputs are evaluated using the MSE algorithm in (4).

is under 120 W/kg for all configurations. It is difficult to analytically estimate the peak SAR_{1g} because of a non-linear function subject to all parameters.

III. ARTIFICIAL NEURAL NETWORK

In the study, three different ANN architectures are implemented to demonstrate the performance: the initial ANN, the ANN with MIV, and the ANN with MIV and GA optimization. For simplicity, the last one is denoted as the ANN using a synthesizing framework.

A fully connected feed-forward neural network was constructed as the initial ANN to fit the local SAR_{1g} near the plate ends and the screw tips. Naturally, the number of input parameters was six, the parameters that used to describe the plate devices. For the outputs, there were three optional choices: 1) SAR_{1g} distributions; 2) local peak SAR_{1g} near possible hotspots; and 3) peak SAR_{1g} . Obviously, the SAR_{1g} distribution was not a feasible choice for the number of the outputs which could be millions. It would make the ANN too difficult to train. Both options 2 and 3 could be used as the outputs, but local peak SAR_{1g} near possible hotspots as output was more robust than the one using the peak SAR_{1g} . This was because the peak SAR_{1g} may occur near different hotspots, thus the relationship between the input and the output was not continuous. This discontinuity will affect the convergence and performance of the ANN. The comparisons of these two choices are discussed in Section VI.

The initial ANN applied in this study consisted of an input layer, two hidden layers, and an output layer, as shown in Fig. 4. Two hidden layers were used because theoretical works have shown that two hidden layers can approximate any smooth mapping to any accuracy [22], [23]. The number of hidden neurons in each hidden layer should be between the number of the neurons in the input layer and the number of the neurons in the output layer [24]. Fewer neurons can lead to underfitting and too many neurons can contribute to overfitting [22], thus five hidden neurons at each layer were chosen for the ANN. As showed in Fig. 4, each neuron in the ANN operates by summarizing its weighted input and the biases and passing to the transfer function [25], and the output of the transfer function is used as the input of the neuron in the next layer. The Tan-sigmoid (Tansig) transfer function is used to transfer the values from the input layer to the hidden layer, and the Purelin linear transfer function is applied to transfer the values of the hidden layers to the output layer.

The nonlinear relationships between the input and output can be accurately characterized by iteratively adjusting the weights w_i and biases b_i based on the training data. The calculation of the neuron's output is shown in the following equations:

$$a^1 = \text{Tansig}(w_1x + b_1) \quad (1)$$

$$a^2 = \text{Tansig}(w_2a^1 + b_2) \quad (2)$$

$$y = \text{Purelin}(w_3a^2 + b_3) \quad (3)$$

where x denotes the vector of the input parameters. w_1 , w_2 , and w_3 are the matrix of connection weights between different layers, while b_1 , b_2 , and b_3 are vectors of the bias for the different layers. a^1 and a^2 are the output vectors, the summarized weighted input and biases in hidden layers. The final output y presents the predicted local peak SAR_{1g}. The performance of the ANN was evaluated with the sum of the mean square error (MSE), which was calculated using (4). In this paper, the lowest validation MSE was used as the best validation performance of the ANN

$$\text{MSE} = \frac{1}{n} \sum_{i=1}^n (y_i - s_i)^2 \quad (4)$$

where s_i denotes the actual peak local SAR_{1g} of the implantable plate device from the simulation results. The data samplings were randomly divided into three groups. About 70% of the whole data were used as training data, 15% were used as validation data, and the rest 15% were used as test data. The Pearson correlation coefficient R [26] was also used to evaluate the performance of ANN where $R = 1$ means a direct positive correlation, and $R = -1$ denotes a direct negative correlation.

Among all training algorithms, Levenberg–Marquardt (LM) has good performance and fast convergence [27], [28]. Thus, to get an efficient and stable ANN, the LM training algorithm was adopted here to train the initial ANN as

$$\text{LM} : w_{k+1} + b_{k+1} = w_k + b_k - [\mathbf{J}^t \mathbf{J} + \mu \mathbf{I}]^{-1} e \quad (5)$$

where \mathbf{J} is the Jacobian matrix containing the first derivatives of the network errors with respect to the weights and biases, and e is the vector of network errors. In this formula, μ is just a parameter (ranges from 0 to 1) that controls the learning rate of the ANN. The Jacobian matrix can be computed through a standard backpropagation technique that is much less complex and more accurate near an error minimum [29].

IV. FEATURE SELECTION WITH THE MIV ALGORITHM

In the initial ANN, all the parameters or features of the implantable plate devices were used as the input of the network. However, the impact of the input on the output of the ANN may be quite different. On one hand, missing noteworthy features may lead to poor performance; on the other hand, overmuch minor features can result in slow convergence and overfitting of the ANN. It is usually very difficult to decide the appropriate features as the input is based on prior information. Thus, to build an efficient and reliable ANN, the MIV algorithm was used to identify the most impactful and import implant features.

The MIV was proposed to select the independent features that had most significant impact on the peak local SAR_{1g}. It has been

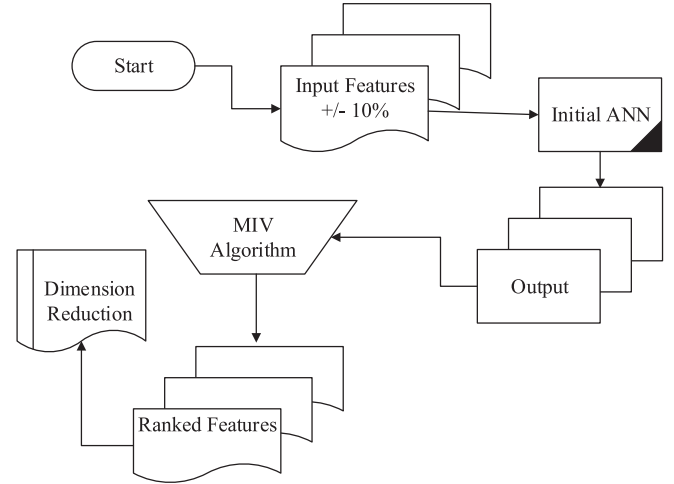


Fig. 5. Flowchart of the feature selection with MIV in ANN.

TABLE II
MIV VALUES OF THE IMPLANTABLE MEDICAL DEVICES

No.	Features	MIV
1	Plate Width	-16.92
2	Distance to 1 st Screw	11.81
3	Screw Diameter	9.84
4	Screw Length	-7.31
5	Plate Length	-4.77
6	Plate Depth	-0.74

considered one of the best indexes to assess the impacts of the input features [30], [31]. As shown in Fig. 5, to get the MIV for the input of the initial ANN, each input feature is added and subtracted by 10% respectively to create two new input features. The MIV of each input feature is calculated by the mean of the different output values. According to the above steps, the MIV of each input feature of the initial ANN is calculated and can get the ranked features, which are given in Table II. The positive or negative MIV values denote that the input is positive or negative correlated to the output. Thus, the absolute MIV shows the relative importance of the input. Finally, the dimension of the input would be reduced according to the ranked features.

As given in Table II, the most impactful features are sorted according to the absolute MIV. The plate depth has the lowest absolute MIV compared to other features, whereas the plate width has the highest absolute MIV = 16.92. The least impactful features would be reduced to a lower dimension or eliminated in the ANN. Thus, it will contribute to a higher efficiency in the prediction of peak local SAR_{1g}. In this study, the least impactful feature had the smallest absolute MIV = 0.75. That means the input barely affects the peak local SAR_{1g}, but it may increase the computation burden and can cause over-fitting problems. Thus, the least important feature, i.e., the plate width, will no longer be used as the input for the ANN.

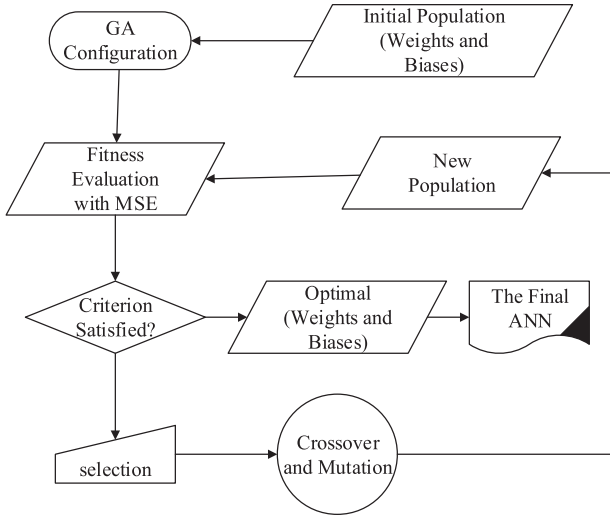


Fig. 6. Flowchart of the ANN optimization with GA. The MSE was utilized to calculate the fitness function. The optimized weights and biases will be updated in the ANN if they have satisfied certain criteria. Otherwise, the GA will keep updating to get its new population via operators like selection, crossover, and mutation.

V. OPTIMIZATION OF THE ANN WITH GA

The weights and biases of the ANN were optimized with GA instead of using the random initialized values. To guarantee the convergence while improving the performance of the ANN, the optimal results from the GA will be used as the initial connection weights and biases for the final ANN.

The ANN can be optimized and improved using the GA [32], [33], a procedure loosely based on evolutionary theory. The combination of GA and ANN contains five major steps and the flowchart is illustrated in Fig. 6.

- 1) The first step is to determine the initial population, which represents the connection weights and biases. The GA code is represented by real numbers.
- 2) The second step is to decide the configuration of the GA. The maximum generation is 50, the size of the population is 10, the crossover rate is 0.2, and the mutation rate is 0.1.
- 3) The third step is to evaluate the fitness of these connection weights and biases of the ANN. Then the objective function MSE shown in (4) is directly used as the fitness function.
- 4) The GA operators such as selection, crossover, and mutation are applied according to the value of fitness. The GA process will stop when the fitness result is satisfied with a certain criterion such as smaller than a predefined value.
- 5) Then the final optimal values of the connection weights and biases in each hidden layer for the final ANN are obtained.

The benefit of the GA is the continual improvement of the fitness function by using different GA operators such as selection, crossover, and mutation. The weights and biases in the hidden layer will keep updating until the fitness of the GA satisfy the stop criterion. Otherwise, they will be saved for future operations in the GA process. As shown in Fig. 7, the GA process

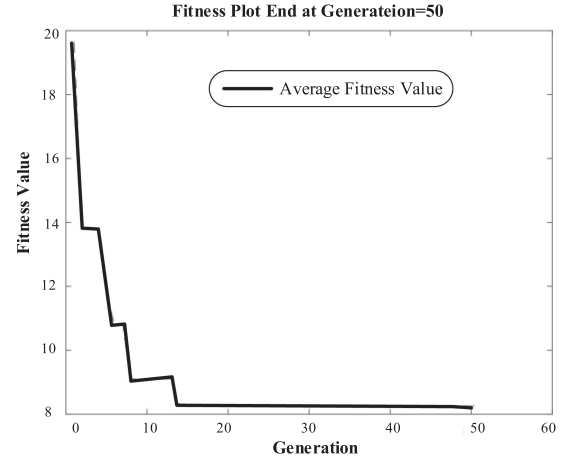


Fig. 7. Plot of fitness results. The objective function MSE shown in (4) was used as the fitness function directly. The fitness value is closed to $8 \text{ W}^2/\text{kg}^2$ after 50 generations, which means the best generation for the weights and biases of the initial ANN was obtained when the lowest MSE value is around $8 \text{ W}^2/\text{kg}^2$.

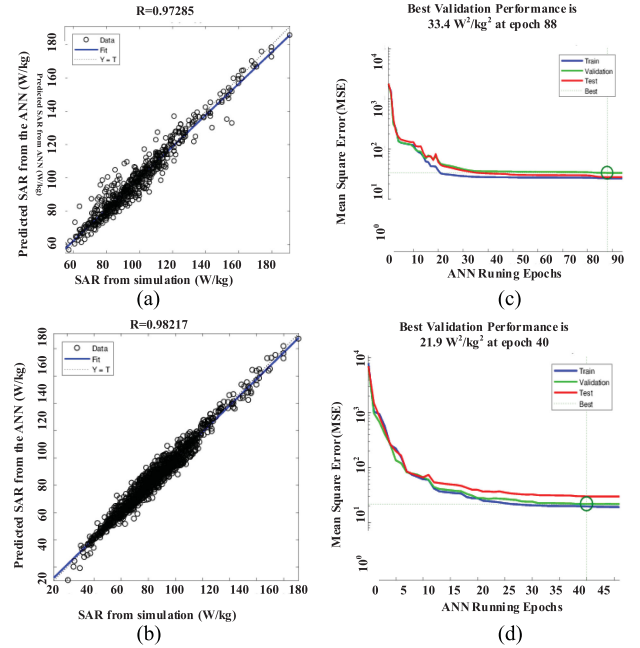


Fig. 8. (a) and (c) Results of the initial ANN with one output which has a correlation coefficient of $R = 0.973$ and a best validation performance of $\text{MSE} = 33.4 \text{ W}^2/\text{kg}^2$. (b) and (d) Results of the initial ANN with two outputs which has a correlation coefficient of $R = 0.982$ and the best validation of $\text{MSE} = 21.9 \text{ W}^2/\text{kg}^2$.

stops after 50 generations when the criterion is satisfied. This means the optimal weights and biases of the ANN are obtained when the lowest $\text{MSE} \approx 8 \text{ W}^2/\text{kg}^2$.

VI. RESULTS AND DISCUSSION

The performances of the initial ANN with one or two outputs were compared to demonstrate the necessity of determining the appropriate outputs. The peak SAR_{1g} on the screw tip was not always lower than at the plate end. Thus, the initial ANN with

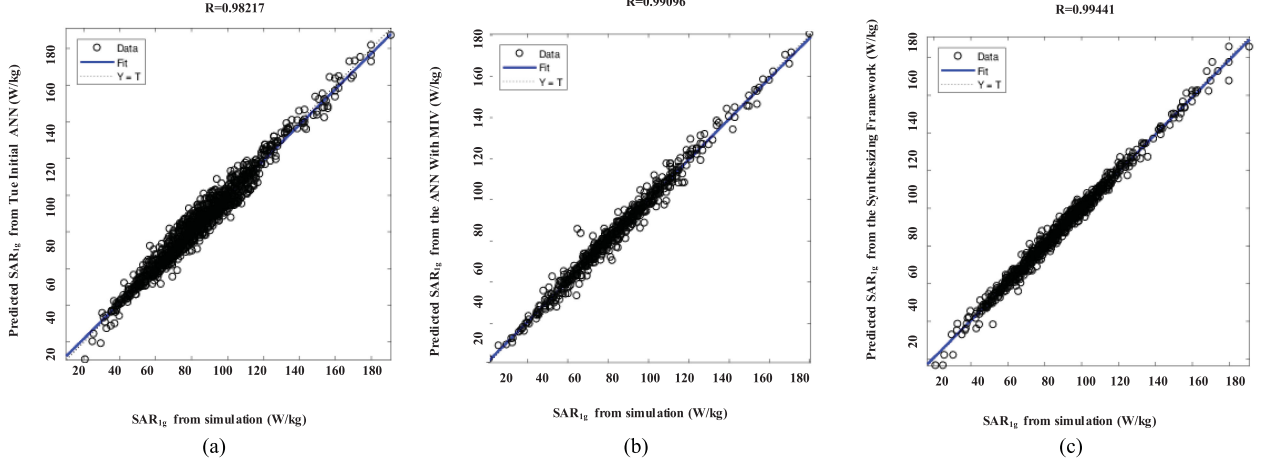


Fig. 9. Comparison of the correlation coefficient between different ANN architectures. The initial ANN has a correlation coefficient of $R = 0.982$. The ANN using the MIV has correlation coefficient $R = 0.991$. The synthesizing framework has a correlation coefficient of $R = 0.994$. (a) Initial ANN. Input: 6 (columns)*576 (rows). Output: 2 (columns)*576 (rows). (b) ANN with MIV. Input: 5 (columns)*576 (rows). Output: 2 (columns)*576 (rows). (c) Synthesizing framework. Input: 5 (columns)*576 (rows). Output: 2 (columns)*576 (rows).

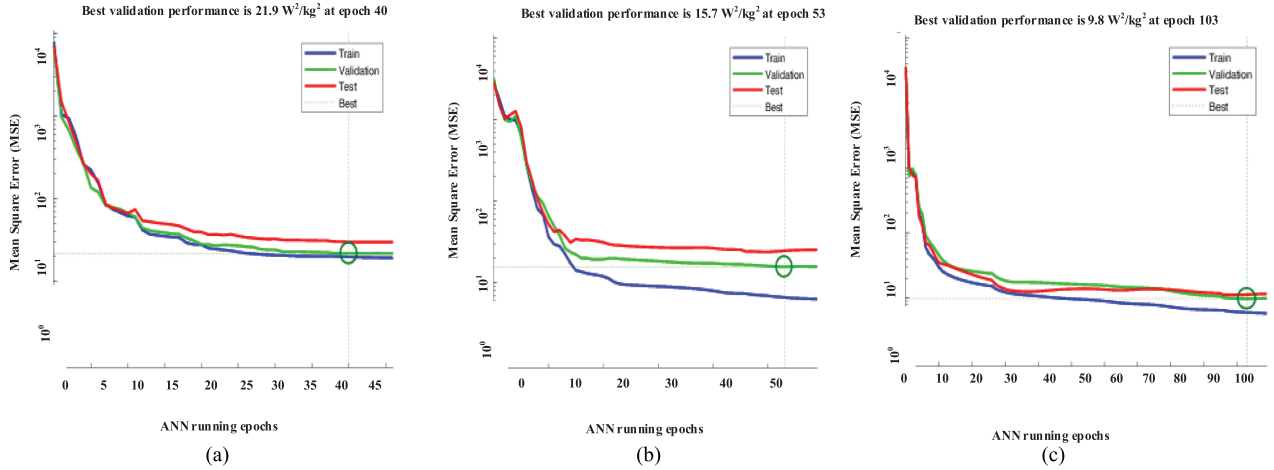


Fig. 10. Comparison of the performance between different ANN architectures. The best validation performance of the initial ANN is $21.9 \text{ W}^2/\text{kg}^2$ at epoch 40. The best validation performance of the ANN with MIV is $15.7 \text{ W}^2/\text{kg}^2$ at epoch 53. The best validation performance of the synthesizing framework is $9.8 \text{ W}^2/\text{kg}^2$ at epoch 103. (a) Initial ANN. Input: 6 (columns)*576 (rows). Output: 2 (columns)*576 (rows). (b) ANN with MIV. Input: 5 (columns)*576 (rows). Output: 2 (columns)*576 (rows). (c) Synthesizing framework. Input: 5 (columns)*576 (rows). Output: 2 (columns)*576 (rows).

two outputs, which were peak $\text{SAR}_{1g, \text{plate}}$ and $\text{SAR}_{1g, \text{screw}}$, was more robust. It showed a stronger correlation between the input features and output peak SAR_{1g} than the ANN with one output. As shown in Fig. 8, the performance of the ANN with two outputs is better than that with one output. The ANN with two outputs approaches a correlation coefficient of $R = 0.982$, and the ANN with one output has a correlation coefficient of $R = 0.973$. The validation performance (the lowest validation MSE value) of the ANN with one output is $\text{MSE} = 33.4 \text{ W}^2/\text{kg}^2$ and the validation performance of the ANN with two outputs is $\text{MSE} = 21.8 \text{ W}^2/\text{kg}^2$. This indicates that the MSE decreased by 34%.

To build an efficient and reliable ANN, the synthesizing framework was further integrated with the MIV feature selection and the GA optimization techniques. First, the most impactful

implant features were identified using the MIV algorithm. Then the GA algorithm was used to optimize the ANN.

Fig. 9 show the correlation coefficient results for the local peak SAR_{1g} of the initial ANN. The predicted local peak SAR_{1g} is slightly varying around the fitting line of $R = 0.982$. The best validation performance is $\text{MSE} = 21.8 \text{ W}^2/\text{kg}^2$, as shown in Fig. 10(a). This also indicates that the error for the predicted local peak SAR_{1g} can be very high using a heuristically constructed ANN. Moreover, the local peak SAR_{1g} was obtained initially from SEMCAD by simulating all different parameters that might take around hundreds of hours. Thus, it is necessary to select the most impactful implant features by using the MIV and improve the efficiency.

We reduced the dimension of features to be only five input features (5×576 data points) for the ANN using the MIV.

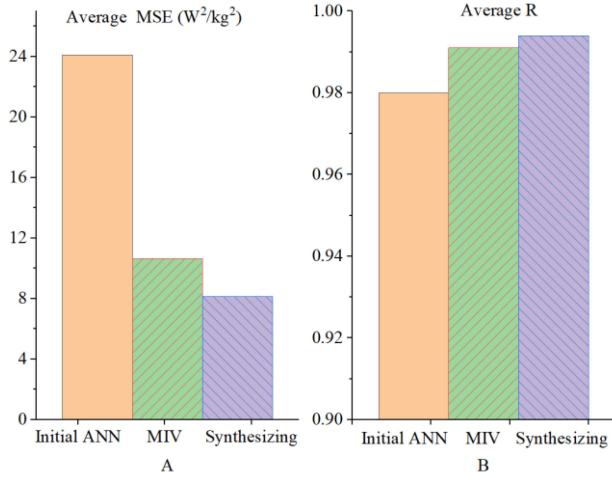


Fig. 11. Comparison of average performance between different ANN architectures. (a) Initial ANN has the highest average MSE value of $24.1 W^2/kg^2$, which means it has the lowest performance. The ANN using the MIV has an average MSE of $10.7 W^2/kg^2$. The synthesizing framework has the best performance which has the lowest MSE value. (b) Initial ANN has a correlation coefficient in average of $R = 0.980$. The ANN using the MIV has a correlation coefficient in average of $R = 0.991$. However, the synthesizing framework has a correlation coefficient in average of $R = 0.994$.

The validated performance MSE was $15.7 W^2/kg^2$, which indicates the MSE decreased by 28%, as shown in Fig. 10(b). The correlation coefficient also increased from 0.982 to 0.991, as shown in Fig. 9.

The synthesizing framework was introduced to improve the performance of the ANN using the most impactful implant features. The performance has been greatly improved, as shown in Figs. 9(c) and 10(c). The simulated and predicted local peak SAR_{1g} are in good consistency and the correlation coefficient is larger than 0.994. The best validation performance is $9.8 W^2/kg^2$, which indicates the MSE decreased by 55%.

Average performance of different ANN architectures was systematically investigated, and the results are shown in Fig. 11. The average performance of the synthesizing framework is the best among the three architectures. The average performance of the initial ANN evaluated by MSE is $24.1 W^2/kg^2$. The average performance of the ANN using the MIV has been improved to obtain $MSE = 10.7 W^2/kg^2$. While it generally takes several hours to calculate the peak SAR_{1g} for the plate devices using a full-wave numerical electromagnetic solver, the ANN can accurately predict the values within microseconds. It is observed that the synthesizing framework is the best model for a fast prediction of the local peak SAR_{1g} .

To further investigate the applicability of the proposed framework, the implant dimensions outside the initial training set were studied. As shown in Fig. 12, the relative errors were small when the implant dimensions were closed to the initial training set. The relative errors were less than 10% when plate length was larger than 300 mm. The screw diameter also showed small relative errors, which were lower than 10% when it increased from 8 to 19 mm. The relative errors were less than 16% when the plate width was either larger than 20 mm or less than 10 mm. Most of the relative errors were less than 21% when the parameter

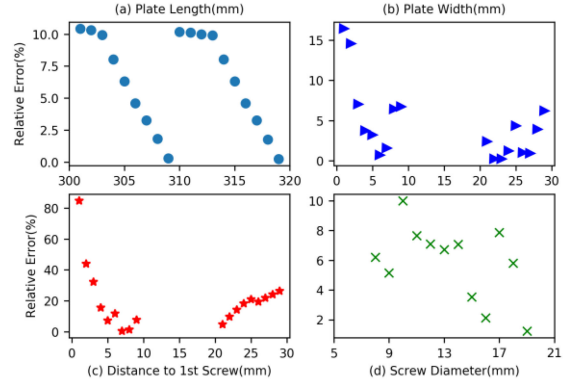


Fig. 12. Relative errors of the predicted results of synthesizing framework compared to simulated results for implant dimensions outside the initial training set. (a) Relative errors were less than 10% when plate length was larger than 300 mm. (b) Relative errors were less than 16% when the plate width was either larger than 20 mm or less than 10 mm. (c) Relative errors became very large if the distance to the first screw was far away from initial training set. (d) Relative errors were less than 10% when the screw diameter was larger than 7 mm.

“distance to first screw” was outside the initial training set. The relative errors became very large if distance to the first screw was far away from initial training set in the range from 1 to 3 mm. However, such small distance to the first screw rarely exists in clinical scenario or real implants. This indicates that the performance of the synthesizing framework will gradually decrease if the distance to the initial training set becomes large. Thus, it was necessary to guarantee the applicability of the framework by providing large-scale dimensions of labeled devices. The two possible hot spots may be different by considering different implantable devices or even with factors related to MRI scanning, such as loading position, devices posture, etc. The synthesizing framework in this study was only consider predicting the local peak SAR_{1g} near the two possible hotspots for the specific plate and screw system under simulation settings shown in Section II. The ANN prediction cannot be used if the hotspot location moves due to significant changes in the device geometry or exposure condition.

VII. CONCLUSION

In this paper, a synthesizing framework was proposed to generate an improved ANN to predict the MRI RF exposure, i.e., the peak SAR_{1g} , of an implantable plate device with screws. The efficiency of the framework and accuracy of the generated ANN was studied numerically. The synthesizing framework was implemented using the MIV algorithm and the GA algorithm to select the most impactful implant features while improving the ANN performance. The MIV was proposed to select the most important implant features based on a heuristically constructed initial ANN. This also served to build an ANN with more flexibility and efficiency. A quick optimization process based on the GA was deployed to determine the connection weights and biases to achieve better performance. Results of synthesizing framework were better than that of the heuristically constructed ANN. It is seen that the proposed framework can improve the efficiency and accuracy of estimating the RF exposure of an implantable medical devices.

In the future, the presented synthesizing framework will be investigated to estimate the RF exposure for more complex and realistic implantable devices. There are three ways to further improve its applicability: First, enlarge the number of labeled devices by providing simulation results of different types of implants; second, extract common features or complex features for different implants that can accurately predict the RF exposure; and third, consider other critical factors related to RF-induced heating, such as loading position, devices orientation, RF coil type, etc.

ACKNOWLEDGMENT

The mention of commercial products, their sources, or their use in connection with material reported herein is not to be construed as either an actual or suggested endorsement of such products by the Department of Health and Human Services.

REFERENCES

- [1] F. G. Shellock, "Radiofrequency energy-induced heating during MR procedure: A review," *J. Magn. Reson. Imag.*, vol. 12, no. 1, pp. 30–36, 2000.
- [2] J. C. Lin, "A new IEEE standard for safety levels with respect to human exposure to radio-frequency radiation," *IEEE Antennas Propag. Mag.*, vol. 48, no. 1, pp. 157–159, Feb. 2006.
- [3] J. Zheng, D. Li, J. Chen, and W. Kainz, "Numerical study of SAR for multi-component orthopaedic hip replacement system during MRI," in *Proc. IEEE Int. Symp. Electromagn. Compat.*, Ottawa, ON, Canada, 2016, pp. 116–120.
- [4] X. Ji, J. Zheng, R. Yang, W. Kainz, and J. Chen, "Evaluations of the MRI RF-induced heating for helical stents under 1.5T MRI system," *IEEE Trans. Electromagn. Compat.*, vol. 61, no. 1, pp. 57–64, Feb. 2019.
- [5] X. Huang *et al.*, "MRI heating reduction for external fixation devices using absorption material," *IEEE Trans. Electromagn. Compat.*, vol. 57, no. 4, pp. 635–642, Aug. 2015.
- [6] D. Li *et al.*, "An efficient approach to estimate MRI RF field induced in vivo heating for small medical implants," *IEEE Trans. Electromagn. Compat.*, vol. 57, no. 4, pp. 643–650, Aug. 2015.
- [7] R. Yang, J. Zheng, W. Kainz, and J. Chen, "Numerical investigations of MRI RF-induced heating for external fixation device in TEM and birdcage body coils at 3 T," *IEEE Trans. Electromagn. Compat.*, vol. 60, no. 3, pp. 598–604, Jun. 2018.
- [8] X. Huang, Z. Wang, J. Chen, and J. Zheng, "Numerical study on MRI RF heating for circular external fixators under 1.5T MRI," in *Proc. IEEE Symp. Electromagn. Compat.*, Long Beach, CA, USA, 2018, pp. 280–285.
- [9] J. Liu *et al.*, "Investigations on tissue-simulating medium for MRI RF safety assessment for patients with active implantable medical devices," *IEEE Trans. Electromagn. Compat.*, pp. 1–7, 2018.
- [10] Q. Zeng *et al.*, "Investigation of RF-induced heating near interventional catheters at 1.5 T MRI: A combined modeling and experimental study," *IEEE Trans. Electromagn. Compat.*, pp. 1–9, 2018.
- [11] *Standard Test Method for Measurement of Radio Frequency Induced Heating On or Near Passive Implants During Magnetic Resonance Imaging*, ASTM 2182-11a, 2011.
- [12] *Assessment of Radiofrequency-Induced Heating in the Magnetic Resonance (MR) Environment for Multi-Configuration Passive Medical Devices*, FDA-2015-D-2104, 2016.
- [13] X. Ji, M. Xia, J. Zheng, J. Chen, and W. Kainz, "Study on the searching strategies of assessing the MRI RF-induced heating for an implantable plate and screw system," in *Proc. IEEE Int. Symp. Electromagn. Compat., IEEE Asia-Pac. Symp. Electromagn. Compat.*, Singapore, 2018, pp. 932–935.
- [14] J. Zheng, X. Ji, W. Kainz, and J. Chen, "Study on search strategies for assessing the worst-case RF-induced heating for multi-configuration implant system under MRI," *IEEE Trans. Electromagn. Compat.*, pp. 1–9, 2018.
- [15] J. Zheng, R. Yang, and J. Chen, "Fast prediction of MRI RF-induced heating for implantable plate devices using neural network," in *Proc. Int. Symp. Antennas Propag.*, San Diego, CA, USA, 2017, pp. 1011–1012.
- [16] X. Ma, Y. Zhang, H. Cao, S. Zhang, and Y. Zhou, "Nonlinear regression with high-dimensional space mapping for blood component spectral quantitative analysis," *J. Spectrosc.*, vol. 2018, 2018, Art. no. 2689750.
- [17] R. Yu, P. Leung, and P. Bienfang, "Predicting shrimp growth: Artificial neural network versus nonlinear regression models," *Aquacultural Eng.*, vol. 32, no. 1, pp. 26–32, 2006.
- [18] G. W. Dombi, P. Nandi, J. M. Saxe, A. M. Ledgerwood, and C. E. Lucas, "Prediction of rib fracture injury outcome by an artificial neural network," *J. Trauma Acute Care Surg.*, vol. 39, no. 5, pp. 915–921, 1995.
- [19] G. Li, H. Alnuweiri, Y. Wu, and H. Li, "Acceleration of back propagation through initial weight pre-training with delta rule," in *Proc. IEEE Int. Conf. Neural Netw.*, 1993, pp. 580–585.
- [20] D. Whitley, "A genetic algorithm tutorial," *Statist. Comput.*, vol. 4, no. 2, pp. 65–85, 1994.
- [21] Reference Manual for the Semcad Simulation Platform for Electromagnetic Compatibility, Antenna Design and Dosimetry, SPEAG, Zurich, Switzerland, 2014.
- [22] S. Karsoliya, "Approximating number of hidden layer neurons in multiple hidden layer BPNN architecture," *Int. J. Eng. Trends Technol.*, vol. 3, no. 6, pp. 714–717, 2012.
- [23] K. Hornik, M. Stinchcombe, and H. White, "Multilayer feedforward networks are universal approximators," *Neural Netw.*, vol. 2, no. 5, pp. 359–366, 1989.
- [24] K. G. Sheela and S. N. Deepa, "Review on methods to fix number of hidden neurons in neural networks," *Math. Probl. Eng.*, vol. 2013, 2013, Art. no. 425740.
- [25] P. D. B. Harrington, "Sigmoid transfer functions in backpropagation neural networks," *Anal. Chem.*, vol. 65, no. 15, pp. 2167–2168, 1993.
- [26] R. Taylor, "Interpretation of the correlation coefficient: A basic review," *J. Diagnostic Med. Sonogr.*, vol. 6, no. 1, pp. 35–39, 1990.
- [27] M. T. Hagan and M. B. Menhaj, "Training feedforward networks with the Marquardt algorithm," *IEEE Trans. Neural Netw.*, vol. 5, no. 6, pp. 989–993, Nov. 1994.
- [28] M. Kayri, "Predictive abilities of Bayesian regularization and Levenberg Marquardt algorithms in artificial neural networks: A comparative empirical study on social data," *Math. Comput. Appl.*, vol. 21, no. 2, pp. 1–11, 2016.
- [29] M. C. Nicoletti, *Computational Intelligence Techniques for Bioprocess Modelling, Supervision and Control*, vol. 218. New York, NY, USA: Springer, 2009.
- [30] F.-Q. Xu and X.-G. Liu, "Variables screening methods based on the optimization of RBF neural network," *Comput. Syst. Appl.*, vol. 3, p. 047, pp. 756–759, 2012.
- [31] Z.-G. Fu, M.-F. Qi, and Y. Jing, "Regression forecast of main steam flow based on mean impact value and support vector regression," in *Proc. Asia-Pac. Power Energy Eng. Conf.*, 2012, pp. 1–5.
- [32] A. Sedki, D. Ouazar, and E. El Mazoudi, "Evolving neural network using real coded genetic algorithm for daily rainfall-runoff forecasting," *Expert Syst. Appl.*, vol. 36, no. 3, pp. 4523–4527, 2009.
- [33] I. Güler, H. Polat, and U. Ergün, "Combining neural network and genetic algorithm for prediction of lung sounds," *J. Med. Syst.*, vol. 29, no. 3, pp. 217–231, 2005.



Jianfeng Zheng (M'13) received the B.S. degree in electronic information engineering and the Ph.D. degree in electronic science and technology both from Tsinghua University, Beijing, China, in 2002 and 2009, respectively.

He was an Assistant Researcher with the State Key Laboratory on Microwave and Digital Communications, Tsinghua University. Since 2012, he has been a Postdoctoral Fellow with the Department of Electrical and Computer Engineering, University of Houston, Houston, TX, USA. His current research interests include applied electromagnetics on biomedical applications, MRI RF safety, MIMO channel measurements, antenna arrays for MIMO communications, etc.



Qianlong Lan received the B.S. degree in network engineering from Shanghai Second Polytechnic University, Shanghai, China, in 2013, and the M.S. degree in computer science from the Texas Southern University, Houston, TX, USA, in 2016. He is currently working toward the Ph.D. degree with the University of Houston, Houston, TX, USA, under Prof. J. Chen's advising.

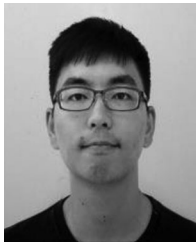
His current research interests include MRI RF safety, remote laboratory, remote control, machine learning, artificial intelligence, and big data.



Wolfgang Kainz (M'03) received the M.S. degree in electrical engineering and the Ph.D. degree in technical science from the Technical University of Vienna, Vienna, Austria, in 1997 and 2000, respectively.

He is currently a Research Biomedical Engineer with the Center for Devices and Radiological Health, U.S. Food and Drug Administration (FDA), Rockville, MD, USA. He has authored/co-authored more than 160 peer-reviewed articles and book chapters. He is a member of the Administrative Committee of the IEEE International Committee on Electromagnetic Safety and a member of many international standard setting committees. After working for the Austrian Research Center Seibersdorf, he joined the Foundation for Research on Information Technologies in Society (IT'IS), Zurich, Switzerland, as the Associate Director. At IT'IS, he worked on the development of *in vivo* and *in vitro* exposure setups for bio-experiments. In 2004, he initiated the Virtual Family Project in co-operation with IT'IS and Prof. J. Chen from the University of Houston. His research interest is currently focused on the safety and effectiveness of medical devices and safety of humans in electromagnetic fields. This includes computational electrodynamics for safety and effectiveness evaluations using anatomical models of the human anatomy; magnetic resonance imaging (MRI) safety; performance and safety of wireless technology used in medical devices; electromagnetic compatibility of medical devices; dosimetric exposure assessments from dc to light; and novel methods to computationally assess the safety and effectiveness of neuroprosthetics and therapeutic stimulation methods.

Dr. Kainz received the prestigious FDA Award of Merit for exceptional leadership in performance in addressing issues of compatibility of medical devices during MRI by applying transparently scientific research to device regulation in 2010.



Xingyao Zhang received the B.S. degree in electronic information engineering from the University of Electronic Science and Technology of China, Chengdu, China, in 2014. He is currently working toward the Ph.D. degree with the University of Houston, Houston, TX, USA, under Prof. X. Fu's advising.

His current research interest lies in the high-performance computing, especially the computer architecture design for machine learning accelerations.



Ji Chen (SM'10) received the B.S. degree from the Huazhong University of Science and Technology, Wuhan, China, in 1989, the M.S. degree from McMaster University, Hamilton, ON, Canada, in 1994, and the Ph.D. degree from the University of Illinois, Urbana-Champaign, IL, USA, in 1998, all in electrical engineering.

He is currently a Professor with the Department of Electrical Engineering, University of Houston, Houston, TX, USA. His research interests include microprocessor full chip-level interconnect extraction, wireless communication system-on-chip interconnect characterization, computer system EMC/EMI modeling, signal integrity analysis, and bioelectromagnetics with applications to MRI systems.

Dr. Chen is a recipient of the ORISE Fellowship in 2006 and the Motorola Engineering Award in 2000.